Primljen / Received: 29.10.2024.
Ispravljen / Corrected: 22.4.2025.
Prihvaćen / Accepted: 2.6.2025.
Dostupno online / Available online: 10.9.2025.

Corrosion deterioration mechanism of fiber-reinforced concrete based on macro- and micro-scale analysis

Authors:

Ya Yin, MCE
18801259880@163.com

Prof. **Lan Qiao**, PhD. CE
lanqiao@ustb.edu.cn

Linbo Song, MSc. ME
1325016164@qq.com

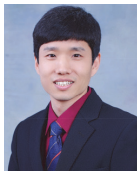

Prof.dr.sc. **Qingwen Li**
qingwenli@ustb.edu.cn
Corresponding author

Miao Miao, MCE
15837090872@163.com

An Luo, MCE
281041645@qq.com

University of Science and Technology Beijing
Faculty of Resources and Security Engineering

Research Paper

Ya Yin, Lan Qiao, Linbo Song, Qingwen Li, Miao Miao, An Luo

Corrosion deterioration mechanism of fiber-reinforced concrete based on macro- and micro-scale analysis

This study systematically investigated the mechanical response and microstructural characteristics of polypropylene fiber-reinforced concrete with prefabricated cracks under simulated field and laboratory corrosion conditions. Six corrosion scenarios were designed based on a C40 concrete mix. Through mechanical testing, digital image correlation, and microstructural characterization, we found that a polypropylene fiber content of 0.3 wt% markedly enhances compressive strength and suppresses lateral deformation, while excessive fiber content leads to performance deterioration due to increased porosity. Higher corrosion concentrations induced a decline in the elastic modulus, although the fiber network mitigated stiffness degradation. Prefabricated cracks promoted the propagation of mixed-mode I–II fractures, with severe corrosion environments significantly increasing microcrack density and advancing the onset of critical strain zones. Microstructural analysis revealed that SO_4^{2-}/Cl^- corrosion decomposes C-S-H gel, generating gypsum, ettringite, and Friedel's salt. This study provides a multiscale theoretical foundation for the corrosion-resistant design and service-life prediction of support structures in deep mining from both macro- and microscale perspectives.

Key words:
fiber reinforced concrete, corrosion deterioration, prefabricated cracks, mechanical properties, DIC, microstructure

Prethodno priopćenje

Ya Yin, Lan Qiao, Linbo Song, Qingwen Li, Miao Miao, An Luo

Mehanizam propadanja betona ojačanog vlaknima uslijed korozije na osnovi analize na makrorazini i mikrorazini

U ovome istraživanju sustavno su ispitani mehanički odziv i mikrostrukturne značajke betona ojačanoga polipropilenskim vlaknima s unaprijed oblikovanim pukotinama, pod simuliranim uvjetima korozije u laboratoriju i na terenu. Osmišljeno je šest scenarija korozije na osnovi betonske mješavine razreda C40. Kombinacijom mehaničkih ispitivanja, digitalne korelacije slike (DIC) i mikrostrukturne analize utvrđeno je da sadržaj polipropilenskih vlakana od 0,3 mas. % znatno poboljšava tlačnu čvrstoću i smanjuje poprečnu deformaciju, dok prekomjerni udio vlakana dovodi do pogoršanja svojstava uslijed povećane poroznosti. Veće koncentracije korozivnih tvari uzrokovale su smanjenje modula elastičnosti, iako je mreža vlakana ublažila degradaciju krutosti. Unaprijed oblikovane pukotine potaknule su širenje mješovitih pukotina tipa I–II, pri čemu su jaki korozivni uvjeti znatno povećali gustoću mikropukotina i ubrzali pojavu kritičnih zona deformacije. Mikrostrukturna analiza pokazala je da korozija uzrokovana ionima SO_4^{2-}/Cl^- razgrađuje kalcij-silikat-hidrat (CSH) gel, pri čemu nastaju gips, etringit i Friedelova sol. Rezultati ovog istraživanja predstavljaju teorijsku podlogu za projektiranje konstrukcija otpornih na koroziju i povećanje njihove trajnosti u uvjetima dubokog iskopa, oslanjajući se na integrirane analize na makrorazini i mikrorazini.

Ključne riječi:
beton ojačan vlaknima, propadanje uzrokovano korozijom, unaprijed oblikovane pukotine, mehanička svojstva, digitalna korelacija slika (DIC), mikrostruktura

1. Introduction

With the advancement of the deep mining of metal deposits, geological structures and ore-body conditions have become increasingly complex [1]. The increase in ground stress, water inflow, sudden water bursts, and severe seepage in well walls have created a challenging environment for high-stress corrosion. Consequently, the surrounding rock and support structures are constantly subjected to the erosive effects of mine water, water pressure, high temperature, and rock stress [2]. Over time, corrosive ions penetrate support structures through cracks and defects, leading to complex chemical reactions that cause deterioration [3, 4]. For instance, Cl^- ions directly induce chemical corrosion in concrete, leading to the dissolution and phase transformation of the cement matrix, accompanied by the formation of expansive Friedel's salt. SO_4^{2-} ions promote the generation of ettringite and gypsum, triggering internal stress concentrations that result in volumetric expansion. Mg^{2+} ions replace Ca^{2+} in the C-S-H gel, forming $Mg(OH)_2$ and increasing porosity. NO^{3-} ions react with C-S-H to produce calcium nitrate, which dissolves the binding phases and facilitates the diffusion of Cl^-. HCO_3^- ions interact with $Ca(OH)_2$ to form soluble $Ca(HCO_3)_2$, accelerating matrix dissolution and intensifying surface spalling. In this harsh environment, the structural integrity of permanent concrete supports in shafts and tunnels significantly diminishes, and durability issues become more pronounced as service life extends and corrosion intensifies [5]. Therefore, in response to the complex geological and engineering conditions unique to deep metal mining, a systematic investigation of the corrosion and deterioration mechanisms of concrete structures within support systems under multiple coupled effects is imperative. Establishing a full life-cycle-oriented framework for preventive maintenance and repair technologies is a critical scientific endeavor to ensure the safety of mining operations and promote sustainable development.

Fibers are widely used as admixtures in concrete for practical engineering projects to significantly enhance their physical and mechanical properties. They effectively fill internal defects, thereby increasing the density, impermeability, and resistance to corrosion [6, 7]. Natarajan et al. [8] demonstrated that concrete specimens with glass fiber contents of 0.09 % and 0.06 % exhibit the highest flexural and shear strengths, respectively. Shi et al. [9] employed two environmentally friendly fiber materials: recycled tire steel fibers (RTSF) and coconut fibers (CF). RTSF primarily contributed to crack resistance, whereas CF enhanced the toughness of the material. Nguyen et al. [10] explored the performance changes of polypropylene fiber concrete under sulfate corrosion and wet-dry cycles, revealing through microscopic tests that the bridging effect of polypropylene within the samples effectively enhanced the resistance of concrete to corrosion and freezing. Driven by practical engineering demands, this study focuses on enhancing the durability of the shaft support concrete system used in mines. Using an in situ concrete mix as the baseline, polypropylene fiber was innovatively introduced as a functional admixture. A systematic gradient experiment on fiber dosage was conducted, incorporating long-term immersion tests, mechanical analysis, and microstructural characterization to thoroughly investigate the mechanisms by which polypropylene fibers enhance the corrosion resistance of concrete.

The issue of joint-induced cracking in shaft wall support structures resulting from non-monolithic construction processes has emerged as a critical bottleneck that limits their long-term load-bearing performance. Existing studies have shown that the initiation and propagation of internal defects and microcracks are the central causes of structural failure [11, 12]. Moreover, the transient impact loads generated by engineering disturbances, such as blasting excavation, further exacerbate crack development and penetration, thereby significantly compromising the overall stability of the support structure [13]. Therefore, this study aimed to investigate the impact of joints and cracks on the strength of support structures through the prefabrication of fissures. In the field of concrete research, scholars have conducted extensive studies on various geometric parameters of cracks, yielding significant results [15, 16]. Xue et al. [17] analyzed the fracture characteristics of prefabricated notched concrete under cyclic loading. Yang et al. [18] examined the dynamic fracture performance of polyvinyl alcohol fiber concrete with prefabricated cracks. Although polypropylene fibers have demonstrated notable advantages in enhancing the corrosion resistance and durability of concrete, the underlying mechanisms by which they improve the corrosion resistance of prefabricated cracked concrete have yet to be elucidated at the microscale. Furthermore, the coupling mechanisms between the corrosion deterioration patterns observed in laboratory-fabricated cracked concrete and those occurring in actual mining environments remain unclear, making it difficult for laboratory findings to directly inform engineering practices.

This study focuses on the shaft support concrete of the Shaling Gold Mine and investigates the corrosion resistance of prefabricated crack polypropylene fiber-reinforced concrete under both field- and laboratory-simulated equivalent corrosion environments. The optimal polypropylene fiber (PF) dosage was determined based on the actual in situ mix proportions. Six distinct corrosion conditions were designed: a fiber-free baseline corrosion group, a fiber-reinforced non-corroded control group, an in situ immersion group, and three accelerated corrosion groups at 1x, 3x, and 6x equivalent concentrations, respectively. Comprehensive macroscopic mechanical tests were conducted and Digital Image Correlation (DIC) was employed to examine the crack propagation characteristics of the prefabricated

fiber-reinforced concrete under uniaxial compression. Scanning Electron Microscopy (SEM) was used to observe the evolution of the microstructural morphology, and X-ray Diffraction (XRD) was used to quantitatively analyze the formation patterns of corrosion products such as Friedel's salt and gypsum. This study reveals the mechanisms of fiber reinforcement and corrosion deterioration from both macro- and microscale perspectives, offering key parameters and theoretical support for the corrosion-resistant design of support structures in high-salinity mines. It also provides a technical reference for the design of working conditions for accelerated indoor corrosion tests.

2. Pilot program design

2.1. Material and proportioning design

This study used a mix design of shaft support concrete to prepare C40 fiber concrete samples. The mix proportions of the C40 concrete used in the site support structure are listed in Table 1. The water-cement ratio was 0.32, with a standard slump of 190 mm. The 7-day and 28-day compressive strengths under standard curing conditions were 40.6 MPa and 51.3 MPa, respectively. The sand ratio was 42 %, and the density was 2421 kg/m³. Portland cement (PO 42.5) was used. The fine aggregate was well-graded Zone II natural river sand, with an apparent density of 2,400 kg/m³, bulk density of 1,540 kg/m³, and a fineness modulus of 2.89. The coarse aggregate consisted of gravel with two different gradations—5 mm–10 mm and 10 mm–20 mm, having apparent densities of 2,670 kg/m³ and 2,700 kg/m³, and tightly packed densities of 1,510 kg/m³ and 1,540 kg/m³, respectively, mixed in a 1:1 ratio. The fibers used were polypropylene fibers, bundled monofilaments with diameters of 30–80 microns, lengths of 6 mm, density of 0.91 kg/m³, elastic modulus of 4.8 GPa, and tensile strength of 486 MPa, partially replacing fine sand at 0.1, 0.2, 0.3, 0.4, and 0.5wt %. The water for mixing the samples is ordinary tap water, conforming to the Standards for Water Use in Concrete (JGJ63–2006).

2.2. Corrosive conditions and prefabricated crevices

To investigate the deterioration effects of high-salinity environments on fiber concrete samples, this study was based on water quality reports from four shafts. Chloride concentrations in the water samples ranged from 8.5×10³ mg/L to 11.0×10³ mg/L, sulfide concentrations ranged from 40 mg/L to 60 mg/L, and pH values were between 6.5 and 8, indicating near-neutral conditions. To ensure experimental accuracy, an equivalent 1x corrosion immersion solution was prepared in the laboratory based on the chloride and sulfate concentrations from the main shaft water reservoir (at a depth of 1100 m). Specifically, the solution contains chloride and sulfate ion concentrations of 9.57×10³ mg/L and 56 mg/L, respectively. To simulate the equivalent corrosion and accelerated corrosion effects of the actual environment, equivalent 3x and 6x corrosion solutions were prepared and compared with non-corrosive and in situ immersion conditions. Because the experiment primarily focused on the effects of chloride and sulfate on sample deterioration, only NaCl and Na_2SO_4 were used to prepare the solutions to exclude interference from other potential corrosive ions. Long-term immersion tests were conducted both on-site and in the laboratory, with an immersion period of 120 days, and non-fiber equivalent 1x corrosion and fiber non-corrosive conditions were set as blank control groups. In summary, six experimental conditions were designed for this study: fiber-free specimens under 1x equivalent corrosion, fiber-reinforced specimens without corrosion, in situ immersion, and accelerated corrosion conditions at 1x, 3x, and 6x equivalents.

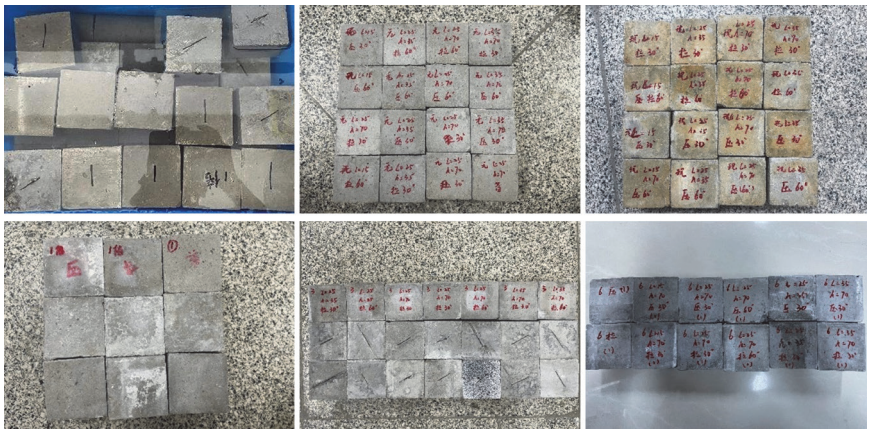

Figure 1. Photographs of the six specimen groups (A1–A6)

Table 1. Concrete proportioning for shaft support

Material name	Cement	Sand	Stone	Water
Parametric	PO 42,5	Fineness modulus 2.8 Mud content 2.6 %	Gradation 5 mm - 25 mm Mud content 0.6%	Natural water
Amount of material (kg/m³): Cement: Sand: Stone: Water = 496: 712: 982: 231				
Weight ratio: Cement: Sand: Stone: Water = 1: 1.44: 1.98: 0.47				

Table 2. Experimental conditions

Condition description	ID	Specimen size [mm]	Crack size [mm]	No. of Specimens				NaCl/(g·L^{-1})	Na_2SO_4 /(g·L^{-1})
				Compression	Tension	Shear	Microstructural		
Fiber-free, 1x equivalent corrosion	A1	70.7×70.7×70.7	70.7×20×1	3	3	3	powder	15.84	0.09
Fiber-reinforced, no corrosion	A2	70.7×70.7×70.7	70.7×20×1	3	3	3	powder	-	-
In situ immersion (on-site)	A3	70.7×70.7×70.7	70.7×20×1	3	3	3	powder	-	-
Lab immersion, 1x concentration	A4	70.7×70.7×70.7	70.7×20×1	3	3	3	powder	15.84	0.09
Lab immersion, 3x concentration	A5	70.7×70.7×70.7	70.7×20×1	3	3	3	powder	47.51	0.27
Lab immersion, 6x concentration	A6	70.7×70.7×70.7	70.7×20×1	3	3	3	powder	95.02	0.54

For ease of data presentation and analysis, the six conditions are hereafter referred to as A1, A2, A3, A4, A5, and A6. The specific parameters are listed in Table 2, and photographs of the specimens are shown in Figure 1.

To analyze the failure patterns of samples with prefabricated fissures under different corrosion immersion environments, a high-precision 3D printer (XYZ Printing Da Vinci 3.0) was used to create the fissures (dimensions 70.7 mm×20 mm×1 mm). The printer has a nozzle diameter of 0.4 mm and a printing precision of 0.1 mm. It operates on the principle of fused deposition modeling (FDM), using polylactic acid (PLA) as the printing material and constructing samples through layered deposition.

2.3. Experimental plan

The experimental scheme used in this study is shown in Figure 2, and the preparation process for the samples with prefabricated fissures is as follows:

- Before casting the specimens, place the 3D-printed solid fissure model (dimensions 70.7 × 20 × 15 mm) into a plastic mold, with the mold's internal dimensions being 70.7 × 70.7 × 70.7 mm.
- Prior to casting, dry the fine and coarse aggregates as required by the Test Methods for Fiber Concrete standard (CECS 13-2009) to ensure the fibers are evenly dispersed in the sample and to avoid clumping.
- According to the predetermined mix proportions, first dry-mix the fine sand and cement for 60 seconds, then add the fiber material into the mixer and continue mixing for 60 seconds.
- Slowly add water along the inner wall of the mixer and mix for 60 seconds. Finally, gradually add the weighed gravel into the mixer and mix for 90 seconds. If clumping occurs during mixing, stop the machine immediately, manually break up the clumps with a spatula, and restart the mixer to continue mixing.
- To ensure smooth demolding, evenly spray a release agent on the fissure model and the inner walls of the mold. After mixing, pour the slurry into the mold in batches, ensuring the fissure is centered and angled at 30° using a protractor, to prevent displacement due to vibration. Scrape off excess mortar and cover with plastic wrap to complete the casting. Once the specimen has set, carefully remove the 3D-printed crack mold. After 48 hours, demold the specimens and place them in a curing chamber at constant temperature and humidity for 28 days. Then, conduct the experiments.

Testing methods are as follows:

- **Mechanical properties test:** Compressive and tensile strength tests were conducted using a WHY-2000Z microcomputer-controlled pressure testing machine according to the Technical Specification for Application of Fiber Concrete (JGJ/T 221-2010). The loading rates were 0.5 MPa/s and 0.05 MPa/s. Direct shear tests were conducted according to the Standard for Geotechnical Testing Methods (GB/T 50123-2023). The specimens were placed in a shear box (sized to fit 70.7 mm) with careful alignment of the shear plane to minimize boundary friction.

Figure 2. Test program

Normal stress was applied in stages, and each stage was maintained for 10 minutes. Subsequently, horizontal shearing was performed at a constant rate (0.5 mm/min) until failure occurred.

- **Extensometer:** Use a circumferential extensometer to measure the Poisson's ratio of the samples (Φ50 mm × 100 mm). The upper and lower surfaces of the sample were ground before loading to ensure flatness was less than 0.5 mm, the dimensional error was within ±0.03 mm, and the vertical error was within ±0.25°. When measuring the Poisson's ratio, the load was applied at a rate of 100 N/s until 80 % of the compressive strength was reached and then switched to a rate of 0.005 mm/min to protect the extensometer.
- **DIC System:** High-speed DIC technology was employed to observe crack propagation. A Photron FASTCAM Nova S12 high-speed camera system (dual synchronized cameras, 1280 × 1024 pixel resolution, 10,000 fps frame rate) was paired with Nikon 24-70 mm f/2.8 lenses (set at 50 mm focal length, f/8.0 aperture). Imaging was conducted at a distance of 700 mm from the 70.7 mm cubic specimens. Data were processed using XTDIC Analyzer Pro 2024 software with a subset size of 31 × 31 pixels, a step size of 5 pixels, and Green-Lagrange strain calculations. Accuracy was ensured through calibration with a 12 × 9 grid board (RMS = 0.012 pixels) and environmental control at a constant temperature of 22 ± 0.5°C.
- **SEM Microscopic Analysis:** The concrete fragments, taken from the mechanical tests, were dried to a constant weight in an electric thermostatic air dryer at 60°C. Gold sputtering was performed on the fresh fracture surface and the microscopic morphology of the stone section was observed using a Hitachi S4800 Scanning Electron Microscope (SEM).
- **XRD Testing:** The concrete fragments, taken from the mechanical tests, were dried in a vacuum oven at 45°C and ground into powder less than 0.08 mm. A Bruker D8 Advance X-ray diffractometer was used to analyze the mineral composition. The scanning speed was 4°/min, with a step size of 0.02° in the diffraction mode, covering a scanning range of 5° to 80°.

2.4. Pre-experiment

The primary objective of the preliminary experiment was to determine the optimal dosage of polypropylene fibers in concrete, thereby providing a scientific basis for subsequent corrosion tests. In this study, concrete specimens with five different fiber dosages were systematically subjected to compressive strength tests. (The results are presented in Figure 3.) The analysis revealed that an appropriate amount of polypropylene fiber significantly enhanced the compressive strength of concrete. However, when the fiber dosage exceeds a certain threshold, the compressive strength begins to decline. A fiber content of 0.3 wt % was identified as the optimal reinforcement ratio. This phenomenon is mainly

attributed to the agglomeration effect caused by excessive fibers within the concrete matrix, which leads to increased porosity and uneven distribution, ultimately compromising the density and overall strength of the concrete. Previous studies on polypropylene fiber-reinforced concrete have reported varying optimal dosages, such as 0.05 %, 0.3 %, and 0.8 % [19], which can be attributed to differences in material properties, concrete mix proportions, experimental conditions, testing methods, and performance indicators. Based on the findings of this study, the final optimal polypropylene fiber dosage was determined to be 0.3wt %. Subsequent studies will focus on analyzing the deterioration mechanisms of fissure-containing concrete under multiple corrosive conditions, mainly from macro- and microscopic perspectives.

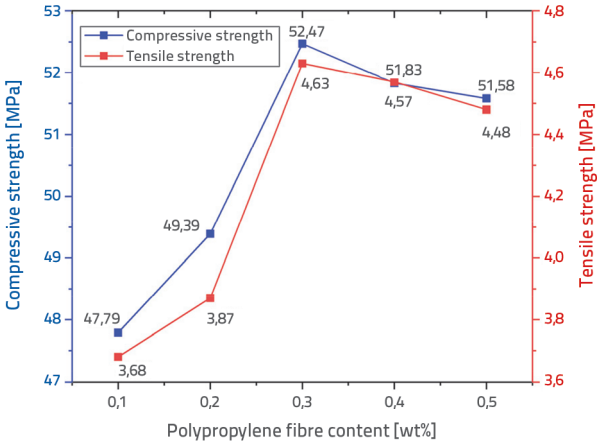

Figure 3. Compressive and tensile strength of concrete with different fiber additions

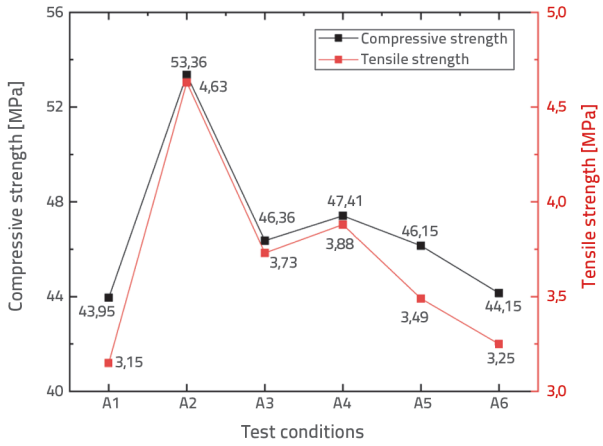

Figure 4. Compressive strength and tensile strength of specimens under different test conditions

3. Results

3.1. Mechanical strength analysis

3.1.1. Compressive and tensile strength

The mechanical tests conducted on the samples under different experimental conditions yielded results for the compressive and tensile strengths, as shown in Figure 4. The compressive strength of samples A1 and A4 increased from 43.95 MPa to 47.41 MPa (a rise of 7.87 %), indicating that fiber addition significantly enhances the anti-corrosion performance of the samples. However, sample A2's compressive strength reached 53.56 MPa, while A3, A5, and A6 showed compressive strengths of 46.36 MPa, 46.41 MPa, and 44.15 MPa under corrosive environments, respectively, all of which decreased. The analysis indicated that the impact of different corrosion immersion environments on the compressive strength varied, with the overall trend showing that as the concentration of the corrosive solution increased, compressive strength decreased. The penetration of Cl^- and SO_4^{2-} ions into the samples triggers complex chemical reactions, producing expansive substances that induce expansion stress and various forms of cracks within the samples [20]. Notably, A3's compressive strength was slightly lower than that of A4, possibly because of the higher average temperature of the underground water (40°C) compared to the laboratory temperature (23°C), which affects the rate at which corrosive ions infiltrate the samples and influences the degree of damage and deterioration [21].

The tensile strength results indicated that the fiber-reinforced samples exhibited higher tensile strengths than those without fibers. The tensile strengths of the samples under the four different corrosion immersion conditions followed the order A4 > A3 > A5 > A6. As the concentration of the corrosion immersion solution increases, the tensile strength of the samples gradually decreases. Overall, the addition of fibers significantly enhanced the tensile strength and anti-corrosion performance of the samples.

3.1.2. Cohesion and angle of internal friction

The direct shear test was employed to determine the shear strength parameters of concrete specimens under applied shear forces, specifically cohesion (c) and internal friction angle (Φ). Φ and c are key parameters of material mechanical properties, directly reflecting the frictional force between particles inside the material and the cohesive force between adjacent portions [22]. The direct shear test was conducted on the specimens using a direct shear test machine, with normal stresses set at 2.5, 5.0, and 7.5 MPa, respectively. After processing and curve fitting the experimental data, the shear stress-strain curves were plotted with normal stress (normal stress) on the x-axis and shear stress on the y-axis, as shown in Figure 5.

Based on the Mohr-Coulomb criterion, the values of Φ and c for the specimens were obtained, as shown in Figure 6. A comparison between specimens A3 and A4 reveals that both exhibit significantly higher Φ and c values than A1, indicating that the surface roughness and irregular shape of the fibers facilitate interlocking with particles, thereby increasing interparticle friction. Under environmental temperature influence, the Φ and c of A3 are lower than those of A4.

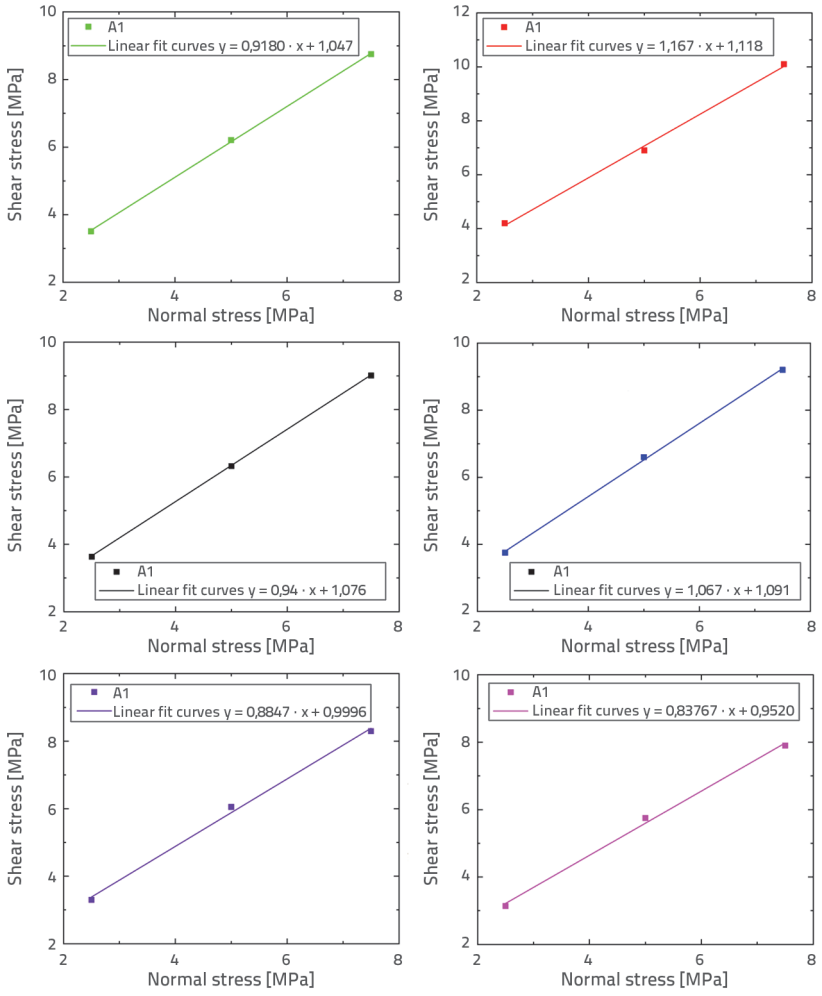

Figure 5. Fitting curves of straight shear test of specimens under different test conditions

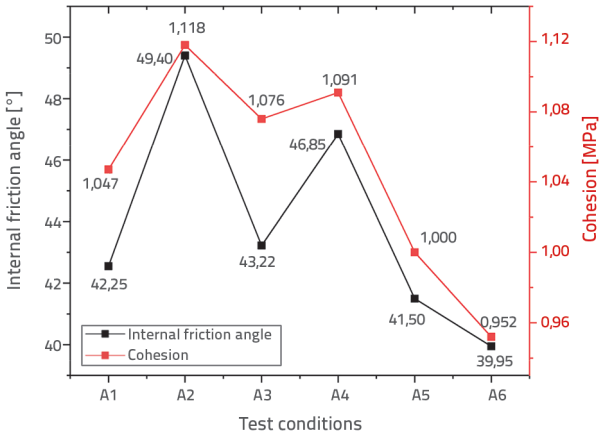

Figure 6. Internal friction angle and cohesion of samples under different test conditions

From the perspective of molecular thermal motion, rising temperatures intensify molecular activity, alter the material's thermal expansion coefficient, weaken interparticle bonding forces, and, consequently, reduce cohesion and lower Φ. Following immersion in corrosive environments, a declining trend in Φ and c was observed. Compared with A4, specimen A5 exhibited a more pronounced deterioration, whereas A6 showed a relatively milder decline, suggesting that the rate of performance degradation slows as the concentration of the corrosive solution increases. In low-concentration environments, the corrosion reactions are relatively mild and primarily affect weak zones on the specimen surface, such as pores between particles and defects on the fiber surfaces. As the solution concentration increases, a denser layer of corrosion products forms on the specimen surface, mitigating the penetration and impact of the reaction on the internal structure.

3.2. Poisson's ratio and modulus of elasticity analysis

The Poisson's ratios and elastic moduli of the specimens were obtained using an extensometer, as shown in Figure 7. As shown in the figure, specimen A2 exhibited the lowest Poisson's ratio, which can be attributed to the high tensile strength and excellent toughness of the polypropylene fibers. When subjected to external loads, the fibers can bear part of the lateral stress, thereby hindering the propagation of internal microcracks and the development of lateral deformation. This effect is akin to forming a microscopic "support network" within the specimen, helping to maintain its shape and dimensional stability. The Poisson's ratios of specimens A3 and A4 were similar, indicating that the influence of the environmental temperature on the Poisson's ratio of the specimens was relatively small. In a corrosive solution, ions chemically react with the surface material of the specimen, damaging the protective layer, increasing the internal porosity, and weakening the bonding strength of the material. Specimen A6 exhibited the highest Poisson's ratio, indicating an enhanced capacity for lateral deformation. This suggests that corrosion not only affects the Poisson's ratio but may also exert a significantly negative impact on the overall mechanical performance and durability of the specimen.

The elastic modulus is an important parameter for measuring material rigidity and is calculated from the elastic stage of the stress-strain curve. As shown in the figure, specimen A2 exhibited the highest and lowest elastic modulus, while A1 showed the lowest. This is attributed to the polypropylene fibers altering the internal structure, thereby enhancing stiffness and strength. The fibers reinforce and toughen the specimen, enabling it to better

resist deformation under load, while also improving its energy absorption capacity and reducing damage. Although specimen A6 had the lowest elastic modulus, it remained higher than that of the specimens without fiber addition, indicating that fiber addition effectively improved the rigidity and overall mechanical performance of the specimens. The elastic moduli of specimens A3 and A5 are similar. As the concentration of the corrosive solution increases, the elastic modulus gradually decreases. However, once corrosion reaches a certain extent, the formation of new chemical reaction products within the specimen leads to the development of new internal structures, thereby slowing the downward trend in the elastic modulus.

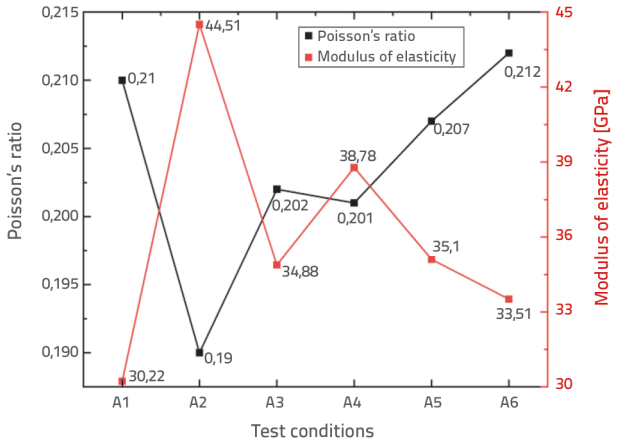

Figure 7. Poisson's ratio and modulus of elasticity of specimens under different working conditions

3.3. Macroscopic damage pattern analysis based on DIC

The fiber-reinforced concrete specimens with pre-existing cracks (length = 15 mm, angle = 30°, and depth = 70 mm) underwent uniaxial compressive testing, and their failure modes are shown in Figure 8. The red and yellow circles indicate prefabricated cracks and primary crack propagation paths, respectively. To analyze the evolution of cracks during loading in depth, four characteristic points (10.0 % Pmax, 48.0 % Pmax, 90 % Pmax, and 99.8 % Pmax) were selected for study. The principal strain and crack propagation trends at each characteristic point were obtained through DIC data processing and are summarized in Table 3. In the initial loading stage (10.0 % Pmax), the internal cracks and defects gradually compacted under pressure, with small principal strains and no concentration phenomena. As the loading progressed to 48.0 % Pmax, strain concentration appeared at the bottom of the pre-existing crack, with differential principal strains forming around the crack and microcrack areas emerging, although macroscopic cracks had not yet formed. Upon reaching 90 % Pmax, the maximum principal strain significantly increased, transferring towards the crack tip where stress concentration occurred, expanding microcrack areas into macroscopic cracks, and approaching specimen failure with stress reaching 85 % to 90 % of the peak strength. Finally, at 99.8 % Pmax, wing cracks and anti-wing cracks formed in the concentrated strain zone, leading to specimen failure. This crack propagation pattern corresponds to a mixed mode of Type I (opening mode) and Type II (shear mode) cracking resulting from the tensile-shear composite stress field induced by compression on the prefabricated cracks in the concrete with a 30° inclination. The crack propagation path deviated from the original fissure axis. The stress concentration at the crack tip triggered symmetric or antisymmetric branching. Wing cracks extended along the direction of the maximum principal stress, whereas anti-wing cracks formed at an obtuse angle to the principal stress direction and were inhibited from further propagation by compressive closure effects. A comparison of the failure patterns depicted in the figure with the above analysis shows that the concentration of the corrosive solution significantly influences the failure mode of the specimen. As the concentration of the corrosive solution increased, the maximum principal strain increased earlier, reaching the critical strain zone sooner, and resulting in earlier and more numerous microcracks. Crack propagation patterns are governed by the combined effects of mechanical loading, material microstructure, and environmental corrosion.

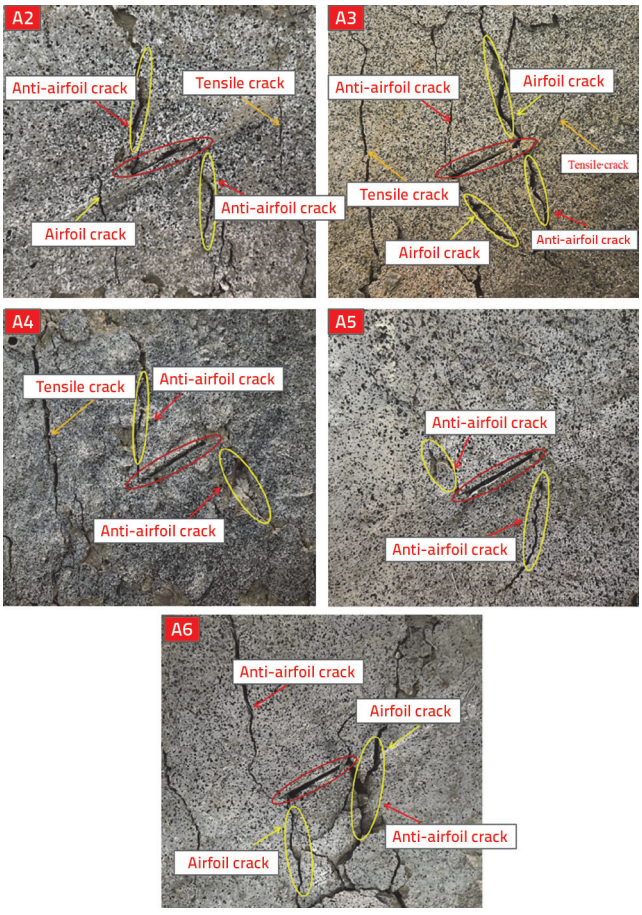

Figure 8. Damage patterns of prefabricated fissure specimens under different test conditionsu različitim ispitnim uvjetima

Table 3. Principal strain clouds of fiber concrete under different test conditions

Test conditions	Feature point 1	Feature point 2	Feature point 3	Feature point 4
A2	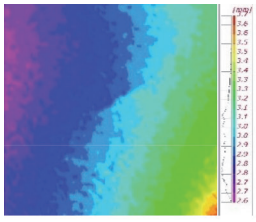	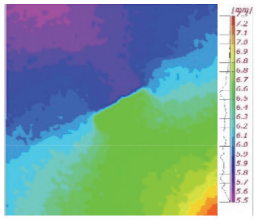	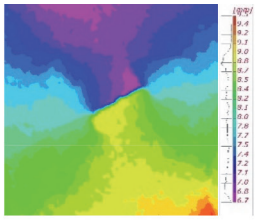	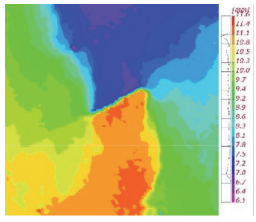
A3	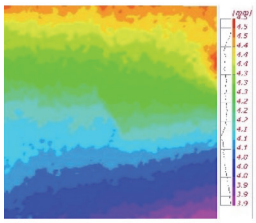	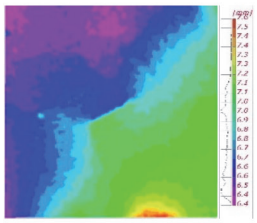	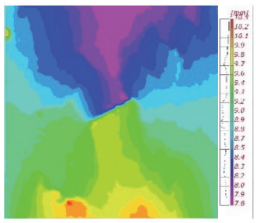	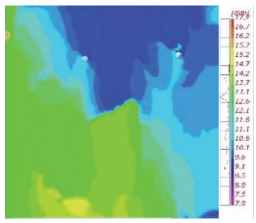
A4	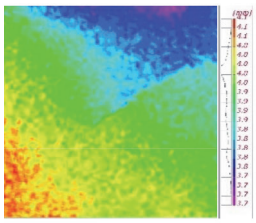	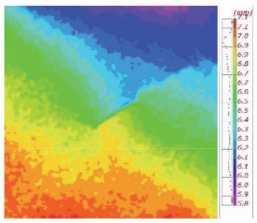	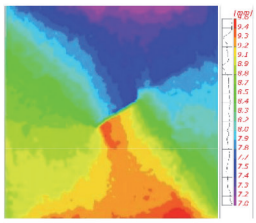	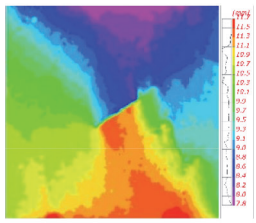
A5	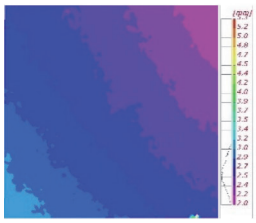	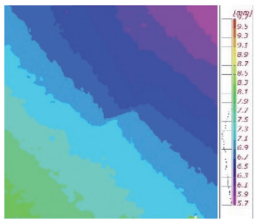	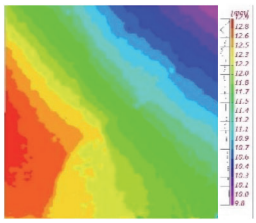	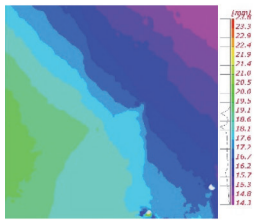
A6	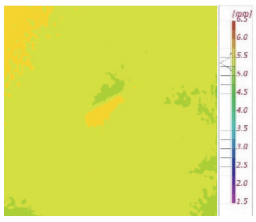	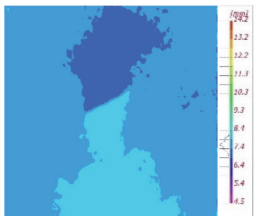	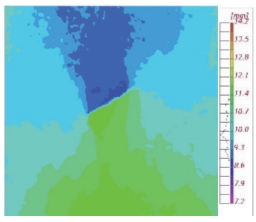	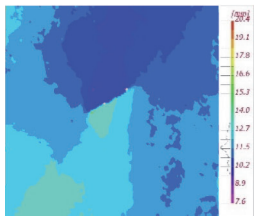

3.4. XRD phase composition

The XRD phase analyses of the powder samples under different test conditions are shown in Figure 9. In the figure, "1" represents quartz (SiO_2), primarily sourced from fine aggregates such as sand and gravel.. "5" represents calcium hydroxide (CH), a hydration product of cement. "7" represents calcium carbonate ($CaCO_3$), mainly from coarse aggregate stones. "2" represents ettringite ($3CaO{\cdot}Al_2O_3{\cdot}3CaSO_4{\cdot}32H_2O$, AFt), and "3" represents gypsum ($CaSO_4{\cdot}2H_2O$), both formed from reactions of SO_4^{2-} infiltrating the samples with cement hydration products. "4" represents Friedel's salt ($3CaO{\cdot}Al_2O_3{\cdot}CaCl_2{\cdot}10H_2O$), formed from reactions of cement hydration products with Cl^-. "6" represents calcium sulfate, formed from reactions between calcium ions in cement and sulfate ions entering the sample.

From A2's XRD curve, it is evident that minimal chloride and sulfate ions were present in the uncorroded sample, with peak intensities showing higher values for CH and lower values for AFt, Friedel's salt, and gypsum. The XRD results for A4 and A6 indicate the appearance of small amounts of gypsum and increasing amounts of AFt and Friedel's salt. CH showed a declining trend, indicating the infiltration of chloride and sulfate ions into the sample, which reacted with C-S-H and CH to form ettringite, filling in cracks and pores. The XRD curves of A4 and A6 show significant decomposition of CH, with SEM scans revealing wide internal cracks due to the expansive products,

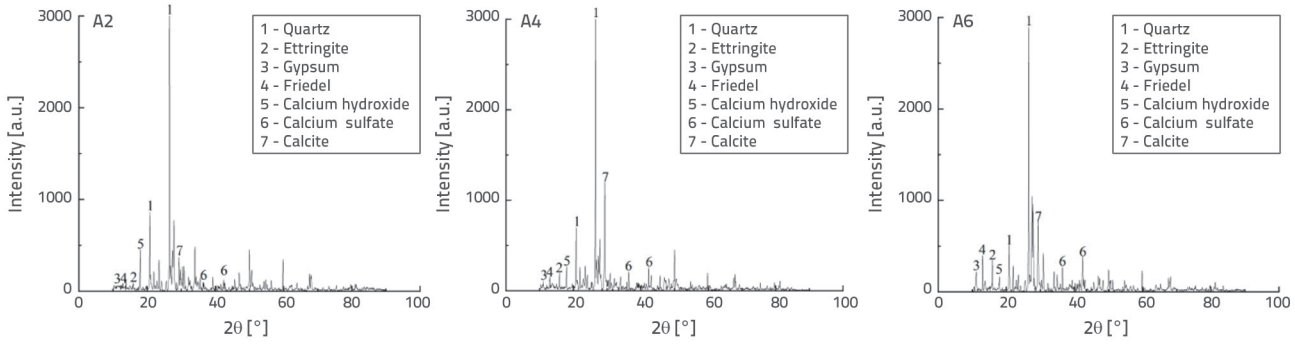

Figure 9. XRD Analysis of the sample

along with abundant white crystals filling these cracks. The peaks for calcium sulfate, AFt, and gypsum continued to increase gradually, indicating ongoing accumulation, although their upward trends were not significant. Conversely, the upward trend of Friedel's salt was notably higher, suggesting that the rate of Friedel's salt formation inside the sample was greater than those of AFt and gypsum, indicating that chloride ions inhibit the formation of sulfate salts to some extent [23]. Furthermore, the increase in Friedel's salt, gypsum, and AFt indirectly correlated with the increased decomposition of cement hydration products, resulting in more defects such as pores and cracks, thereby weakening the bond between the cementitious material and aggregates.

3.5. SEM microstructure

SEM scans of the fiber-reinforced concrete under different test conditions are shown in Figure 10. A2's microstructural features show that before corrosion, the hydration products of the cement in the concrete formed flaky and flocculent C-S-H, as well as thin sheet-like $Ca(OH)_2$. The fibers were well-bonded to the cement matrix, showing no signs of fiber separation or detachment, thereby effectively reinforcing the sample. An appropriate amount of polypropylene fibers improved the structure of the sample, reducing the internal porosity and filling cracks to make the sample denser. Under external loading, polypropylene fibers bridge the surrounding aggregates and cementitious materials, inhibiting the initiation and propagation of microcracks and macrocracks, thereby optimizing the physical and mechanical properties of the sample and enhancing its corrosion resistance. Because of the low diffraction peaks of Friedel's salt and gypsum, SEM did not reveal them in the sample.

As the corrosion immersion concentration increases, the microstructural features of A4 cause severe internal damage to the samples. The chloride and sulfate ions gradually reacted with the hydration product, C-S-H. Various quantities of needle- and rod-like ettringite, gypsum, and Friedel's salt appeared inside the sample and were mainly concentrated in the internal cracks and voids. The microstructural features of A6 show that with an increase in the corrosive solution concentration, the microcracks and micropores expand into larger-scale corrosion pits. In addition to the abundant ettringite, large quantities of columnar and sheet-like gypsum aggregated inside the corrosion pits. The sample exhibited wider cracks internally, where enlarged views failed to observe the morphology of ettringite and gypsum owing to extensive encasement by large quantities of white sodium sulfate and sodium chloride crystals. This indicates that when the corrosive solution concentration increases sixfold, a large number of corrosive ions penetrate the sample and deposit crystalline substances within the defects.

4. Conclusion

This study explored the corrosion resistance of polyethylene fiber-reinforced concrete under prefabricated crack conditions in simulated field and laboratory corrosion

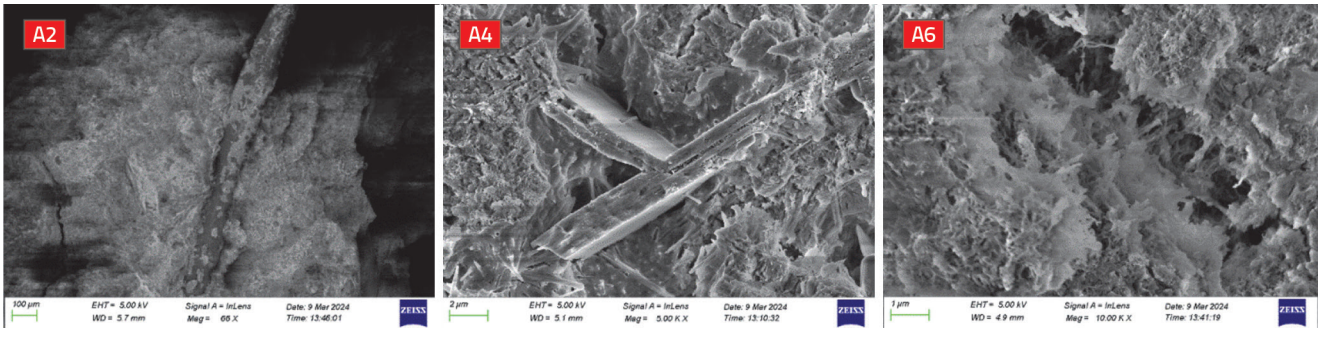

Figure 10. SEM Micrograph of the sample

environments. The experimental conditions were designed under six groups of corrosion scenarios:

- no fiber with equivalent 1× corrosion (A1)
- fiber-reinforced without corrosion (A2)
- in situ immersion (A3)
- equivalent 1× corrosion (A4)
- 3× corrosion (A5)
- 6× corrosion (A6).

This study investigated the mechanical properties of concrete specimens, including compressive strength, tensile strength, and shear strength, as well as the damage and failure behavior under prefabricated fracture conditions, accompanied by a micro-mechanism analysis using XRD and SEM. The following conclusions were drawn.

Based on the support structure of the vertical shaft concrete, C40 fiber-reinforced concrete showed optimal strength with a 0.3wt % addition of polypropylene fibers. Excessive fibers lead to voids and uneven distribution, affecting the compactness and strength of the concrete.

Mechanical tests indicated that the fiber-reinforced concretes (A3 and A4) outperformed the non-fiber-reinforced concrete (A1) in terms of compressive strength, tensile strength, internal cohesion, and internal friction angle. As the corrosion concentration increased, the reduction in these parameters gradually decreased, with the declining trend from A4 to A6 becoming milder. A2 exhibited the smallest Poisson's ratio and the highest elastic modulus, indicating that polypropylene fibers reduce lateral expansion and enhance rigidity. As the corrosion concentration increased, Poisson's ratio increased, and the elastic modulus gradually decreased, but with a mitigating trend.

The uniaxial compressive failure morphology of the prefabricated crack fiber-reinforced concrete, as indicated by the DIC data, showed consistent patterns. The crack propagation mode was a mixed-type crack, combining Mode I (opening-type crack) and Mode II (shear-type crack). This is due to the prefabricated fracture (with a 30° inclination) in the concrete, where the crack is subjected to a tensile-shear combined stress field under compression. Higher corrosion solution concentrations led to greater principal strains, earlier attainment of critical strain regions, and earlier formation of numerous microcracks.

The XRD phase and SEM microstructural analyses revealed that the PFs improved the internal structure of the samples, acting as a reinforcement. With increasing corrosion immersion concentration, C-S-H and CH gradually decomposed, and the quantities of gypsum, Friedel's salt, and ettringite increased. Elevated immersion temperatures exacerbate the decomposition of cementitious materials and increase the size of internal defects. The generation of Friedel's salt inhibited the formation of ettringite and gypsum, demonstrating that chloride ions inhibited sulfate to some extent.

This study provides abundant experimental data and a theoretical basis for investigating the corrosion resistance of fiber-reinforced concrete under prefabricated fracture conditions. Future research can further expand its application fields, optimize the mix design and preparation processes, and improve its durability and reliability. In terms of experimental implementation, tests A1 and A2 are relatively simple, as they mainly involve setting control conditions with or without fiber addition and minimal corrosion exposure. In contrast, the A3 method is more complex because the immersion process is conducted in a field environment.

Acknowledgments

This work was supported by the National Natural Science Foundation of China (52274107, 52204091, and 52374113), Excellent Youth Team Project for the Central Universities (FRF-EYIT-23-01), and the Beijing Nova Program (20230484242).

REFERENCES

[1] Wang, Y., Wu, A., Yang, J., et al.: Progress and prospective of the mining key technology for deep metal mines, Chinese Journal of Engineering, 45 (2023) 8, pp. 1281-1292.

[2] Cai, M., Tan, W., Wu, X., et al.: Current situation and development strategy of deep intelligent mining in metal mines, The Chinese Journal of Nonferrous Metals, 31 (2021) 11, pp. 3409–3421.

[3] Zhu, J., Zhang, Q., Chen, Y., et al.: Progress of Study on Erosion-corrosion, Journal of Chinese Society for Corrosion and Protection, 34 (2014) 3, pp. 199-210.

[4] Li, J., Qiao, J., Fu, X., et al.: Research Progress on Material/Structure and Mechanical Properties of Energy-absorbing Bolt Used in Ground Anchorage, Materials Reports, 33 (2019) 9, pp. 1567-1574.

[5] Sun, L.: Study on failure mechanism and control of high stress and soft rock roadway support, Coal Engineering, 50 (2018) 12, pp. 46-49.

[6] Guo, X.: Study on Tensile Properties of Polypropylene Fiber Concrete, Journal of Xi'an Technological University, 41 (2021) 6, pp. 644-648.

[7] Liang, N., Dai, J., Liu, X., et al.: Experimental study on the fracture toughness of concrete reinforced with multi-size polypropylene fibres, Magazine of Concrete Research, 71 (2019) 9, pp. 468-475.

[8] Natarajan, S., Murugesan, A., Dhanapal, J., Narayanan, A.: Glass fiber reinforced ultra-high strength concrete with silica fume , GRAĐEVINAR, 74 (2022) 10, pp. 849-856, https://doi.org/10.14256/JCE.3431.2021

[9] Shi, H., Shi, Z., Zhang, B., Chen, H.: Investigating the effect of green hybrid fibre on toughening and mechanical properties of iron-tailing sand concrete, GRAĐEVINAR, 76 (2024) 10, pp. 931-942, https://doi.org/10.14256/JCE.4042.2024

[10] Nguyen, H., Kinnunen, P., Carvelli, V., et al.: Durability of ettringite-based composite reinforced with polypropylene fibers under combined chemical and physical attack, Cement and Concrete Composites, 102 (2019), pp. 157-168.

[11] Fan, L.F., Wu, Z.J:. Evaluation of stress wave propagation through rock mass using a modified dominate frequency method, Journal of Applied Geophysics, 132 (2016), pp. 53–59.

[12] Ding, X., Xiao, X., Wu, D., et al.: Study on failure of brittle solids with circular hole and internal crack based on 3D-ILC, Materials Reports, 35 (2021) 18, pp. 18096-18103.

[13] Kušter Marić, M., Ivanović, A., Fusić, M., et al.: Experimental Investigation of the Explosion Effects on Reinforced Concrete Slabs with Fibers, Buildings, 14 (2024) 4, pp. 1080.

[14] Wu, X., Fang, H., Pan, .J, et al.: Experimental study on dynamic mechanical failure characteristics of concrete specimens with cracks of different angles, Journal of Vibration and Shock, 43 (2024) 4, pp. 142-149+189.

[15] Fang, Z., Zhang, Q., Niu, L., et al.: Experiment on evolution law of strain field and temperature field of cracked concrete, Science Technology and Engineering, 21 (2021) 34, pp. 14726-14733.

[16] Dayyani, M., Mortezaei, A., Rouhanimanesh, M. S., Marnani, J. A.: Performance of reinforced engineered cementitious composite square columns, GRAĐEVINAR, 75 (2023) 1, pp. 31-21, https://doi.org/10.14256/JCE.3503.2022

[17] Xue, X., Liu, H.: Fracture Characteristics Test of Precast Concrete Cracks Under Cyclic Loading, Safety in Coal Mines, 50 (2019) 11, pp. 72-75.

[18] Yang, G., Li, F., Zhang, Z., et al.: Experimental Study on Dynamic Fracture Process of Polyvinyl Alcohol Fiber Concrete, Bulletin of the Chinese Ceramic Society, 42 (2023) 2, pp. 454-462.

[19] Luo, Y., Yu, F.: A Review of Research on Fiber-Reinforced Concrete, Journal of Jiamusi University (Natural Science Edition), 42 (2024) 10, pp. 122-124.

[20] Ding, Q., Gao, Y., Hou, W., et al.: Influence of Cl- Concentration on Corrosion Behavior of Reinforced Concrete in Soil, Journal of Chinese Society for Corrosion and Protection, 41 (2021) 5, pp. 705-711.

[21] Yang, Y., Tan, K., Qin, Y:. Review of Research on the Influencing Factors of Chloride Ion Diffusion in Concrete, Materials Reports, 35 (2021) 13, pp. 13109-13118.

[22] Cong, Y., Kong, L., Zheng, Y., et al.: Experimental study on shear strength of concrete, Concrete, (2015) 5, pp. 40-45.

[23] Geng, O., Sun, Q., Li, D.: Study on Inhibitory Effect of Chlorine Salt on Sulfate Corrosion of Recycled Concrete, Journal of Architecture and Civil Engineering, 37 (2020) 6, pp. 108-116.